magnitude too slow to produce v-weakening, except perhaps at temperatures of 500° to 700°C reached in experiments at coseismic slip velocities (*4*, *5*, *14*, *19*).

The internal polycrystalline substructure of the nanospherules and nanofibers that we observed bears a striking similarity to microstructures found in shocked ductile metals (*24*). As in metals, the well-known ductility of calcite (*25*) may allow the ~5- to 20-nm substructure to form by progressive development of nano–cell walls from dense dislocation networks generated by crystal plasticity. Plastic deformation, fracturing, and abrasion presumably generated the observed nanospherules from the starting "gouge." To explain the chaining of nanospherules, producing the observed fiber structure and CPO, we note that oriented attachment at coherent nanoparticle interfaces is widely reported as a mechanism by which nanocrystallites can rapidly coalesce to form single crystals (*26*, *27*), also in calcite (*28*). On this basis, we suggest that the strong anisotropy in the surface energy of calcite produced similar preferred sintering (neck growth) at high-energy crystallographic interfaces between neighboring spherules (Fig. 3, B and C), leading to dynamic chaining and alignment of the lowest-energy (104) plane (*29*) parallel to the shear plane, and thus to the observed fibrous structure and CPO.

In principle, the mechanism of frictional slip that we propose (Fig. 3, A to C, and fig. S1) is similar to the Ashby-Verrall model for superplasticity by diffusion-accommodated grain boundary sliding (GBS) (Fig. 3D) (*30*), but allows for frictional GBS and for intergranular cavitation (porosity generation by dilatation) when diffusive mass transport is too slow to accommodate GBS. Our findings imply that nanocrystalline PSZs developed in calcite faults can produce v-weakening, and hence seismogenic fault friction, by a mechanism of cooperative nanogranular or nanofiber flow plus diffusive mass transfer (Fig. 3, A to C), even in the upper crust where temperatures are generally considered too low to support diffusion or superplasticity at active fault slip rates. The reason that these processes are observed in our experiments is because diffusive mass transfer is dramatically accelerated by the nanogranular nature of the slip-zone rock that forms, and by water-enhanced grain boundary diffusion. A similar mechanism can also be envisaged to operate at coseismic slip rates, where the high temperatures generated will promote solid-state diffusion. Given the abundant recent observations of nanogranular fault surfaces in tectonically active terrains (*1*–*7*), and the anomalously high rates of diffusion found in nanomaterials (*15*, *16*), the proposed mechanism may be relevant not only to faults cutting calcite-rich rocks such as limestones, but to crustal seismogenesis in general.

REFERENCES AND NOTES

1. J. S. Chester, F. M. Chester, A. K. Kronenberg, *Nature* **437**, 133–136 (2005).
2. K.-F. Ma *et al.*, *Nature* **444**, 473–476 (2006).
3. S. Siman-Tov, E. Aharonov, A. Sagy, S. Emmanuel, *Geology* **41**, 703–706 (2013).
4. S. A. F. Smith *et al.*, *Geology* **41**, 63–66 (2013).
5. M. Fondriest *et al.*, *Geology* **41**, 1175–1178 (2013).
6. J. D. Kirkpatrick, C. D. Rowe, J. C. White, E. E. Brodsky, *Geology* **41**, 1015–1018 (2013).
7. J. P. Evans, M. R. Prante, S. U. Janecke, A. K. Ault, D. L. Newell, *Geology* **42**, 623–626 (2014).
8. C. H. Scholz, *Nature* **391**, 37–42 (1998).
9. B. A. Verberne, C. He, C. J. Spiers, *Bull. Seismol. Soc. Am.* **100**, 2767–2790 (2010).
10. B. A. Verberne *et al.*, *Geology* **41**, 863–866 (2013).
11. B. A. Verberne *et al.*, *Pure Appl. Geophys.* **171**, 2617–2640 (2014).
12. X. Chen, A. S. Madden, B. R. Bickmore, Z. Reches, *Geology* **41**, 739–742 (2013).
13. R. Han, T. Hirose, T. Shimamoto, Y. Lee, J.-i. Ando, *Geology* **39**, 599–602 (2011).
14. G. Di Toro *et al.*, *Nature* **471**, 494–498 (2011).
15. R. Würschum, S. Herth, U. Brossmann, *Adv. Eng. Mater.* **5**, 365–372 (2003).
16. S. C. Tjong, H. Chen, *Mater. Sci. Eng. Rep.* **45**, 1–88 (2004).
17. A. R. Niemeijer, C. J. Spiers, *J. Geophys. Res.* **112**, B10405 (2007).
18. Materials and methods are available as supplementary materials on *Science* Online.
19. K. Oohashi *et al.*, *Geology* **42**, 787–790 (2014).
20. C. J. Spiers, S. De Meer, A. R. Niemeijer, X. Zhang, in *Physicochemistry of Water in Geological and Biological Systems – Structures and Properties of Thin Aqueous Films*, S. Nakashima, C. J. Spiers, L. Mercury, P. A. Fenter, M. F. Hochella Jr, Eds. (Universal Academy Press, Tokyo, 2004), pp. 129–158.
21. X. Zhang, C. J. Spiers, C. J. Peach, *J. Geophys. Res.* **115**, B09217 (2010).
22. J.-P. Gratier, D. K. Dysthe, F. Renard, *Adv. Geophys.* **54**, 47–179 (2013).
23. J. R. Farver, R. A. Yund, *Contrib. Mineral. Petrol.* **123**, 77–91 (1996).
24. N. R. Tao *et al.*, *Acta Mater.* **50**, 4603–4616 (2002).
25. L. A. Kennedy, J. C. White, *Geology* **29**, 1027–1030 (2001).
26. R. L. Penn, J. F. Banfield, *Science* **281**, 969–971 (1998).
27. H. Zhang, J. F. Banfield, *CrystEngComm* **16**, 1568–1578 (2014).
28. N. Gehrke, H. Cölfen, N. Pinna, M. Antonietti, N. Nassif, *Cryst. Growth Des.* **5**, 1317–1319 (2005).
29. N. H. de Leeuw, S. C. Parker, *J. Chem. Soc. Faraday Trans.* **93**, 467–475 (1997).
30. M. F. Ashby, R. A. Verrall, *Acta Metall. Mater.* **21**, 149–163 (1973).

ACKNOWLEDGMENTS

We thank A. Niemeijer, J. Chen, V. Toy, and H. de Bresser. H. King is thanked for the AFM measurements and P. van Krieken for the thermogravimetric analysis. B.A.V. was supported by grant 2011-75, awarded by the Netherlands Research Centre for Integrated Solid Earth Sciences; O.P. by Veni grant 863.13.006, awarded by the Netherlands Organisation for Scientific Research (NWO); and D.A.M.D.W. by ISES grant 2011-74. NWO funded the FIB-SEM. All data are available in the supplementary materials.

SUPPLEMENTARY MATERIALS

www.sciencemag.org/content/346/6215/1342/suppl/DC1
Materials and Methods
Supplementary Text
Figs. S1 to S8
Tables S1 to S2
References (*31*–*40*)

21 July 2014; accepted 11 November 2014
10.1126/science.1259003

SOLID STATE THEORY

Quantum spin Hall effect in two-dimensional transition metal dichalcogenides

Xiaofeng Qian,[1]* Junwei Liu,[2]* Liang Fu,[2]† Ju Li[1]†

Quantum spin Hall (QSH) effect materials feature edge states that are topologically protected from backscattering. However, the small band gap in materials that have been identified as QSH insulators limits applications. We use first-principles calculations to predict a class of large-gap QSH insulators in two-dimensional transition metal dichalcogenides with 1T′ structure, namely, 1T′-MX_2 with M = (tungsten or molybdenum) and X = (tellurium, selenium, or sulfur). A structural distortion causes an intrinsic band inversion between chalcogenide-*p* and metal-*d* bands. Additionally, spin-orbit coupling opens a gap that is tunable by vertical electric field and strain. We propose a topological field effect transistor made of van der Waals heterostructures of 1T′-MX_2 and two-dimensional dielectric layers that can be rapidly switched off by electric field through a topological phase transition instead of carrier depletion.

The discovery of graphene (*1*) has fuelled vigorous investigation of two-dimensional (2D) materials (*2*), revealing a wide range of extraordinary properties (*3*–*5*) and functionalities (*6*, *7*). Owing to their atomic thickness, 2D materials can be horizontally patterned through chemical and mechanical techniques (*8*). Moreover, the weak van der Waals (vdW) interaction between adjacent layers enables vertical stacking of different 2D materials, forming vdW heterostructures (*9*), which offer unprecedented opportunities for exploring quantum electronics at the nanoscale.

[1]Department of Nuclear Science and Engineering and Department of Materials Science and Engineering, Massachusetts Institute of Technology, Cambridge, MA 02139, USA.
[2]Department of Physics, Massachusetts Institute of Technology, Cambridge, MA 02139, USA.
*These authors contributed equally to this work. **†Corresponding author. E-mail: liangfu@mit.edu (L.F.); liju@mit.edu (J.L.)**

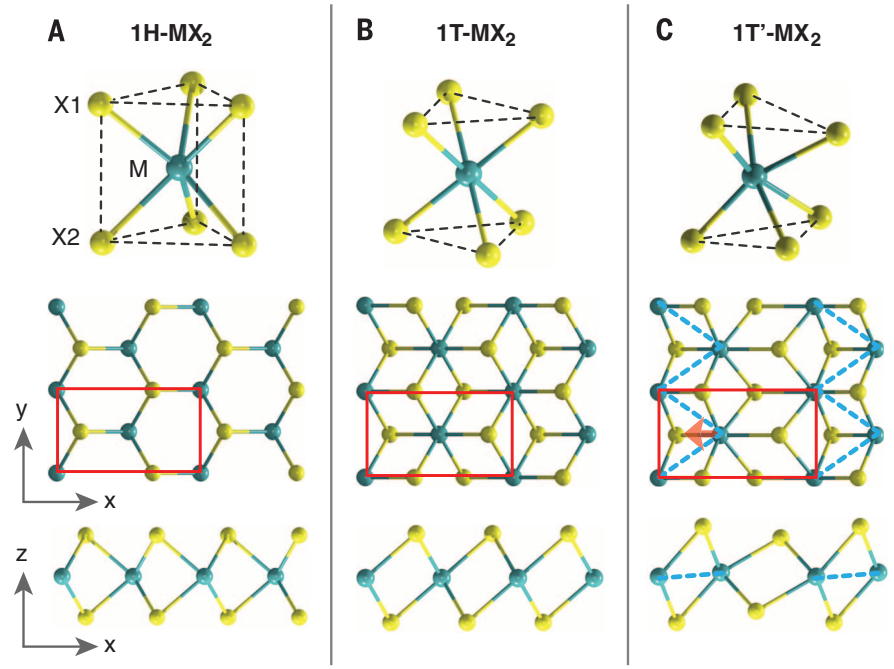

Fig. 1. Atomistic structures of monolayer transition metal dichalcogenides MX_2. M stands for (W, Mo) and X stands for (Te, Se, S). (**A**) 1H-MX_2 in ABA stacking with $P\bar{6}m2$ space group. (**B**) 1T-MX_2 in ABC stacking with $P\bar{3}m2$ space group. (**C**) 1T′-MX_2, distorted 1T-MX_2, where the distorted M atoms form 1D zigzag chains indicated by the dashed blue line. The unit cell is indicated by red rectangles.

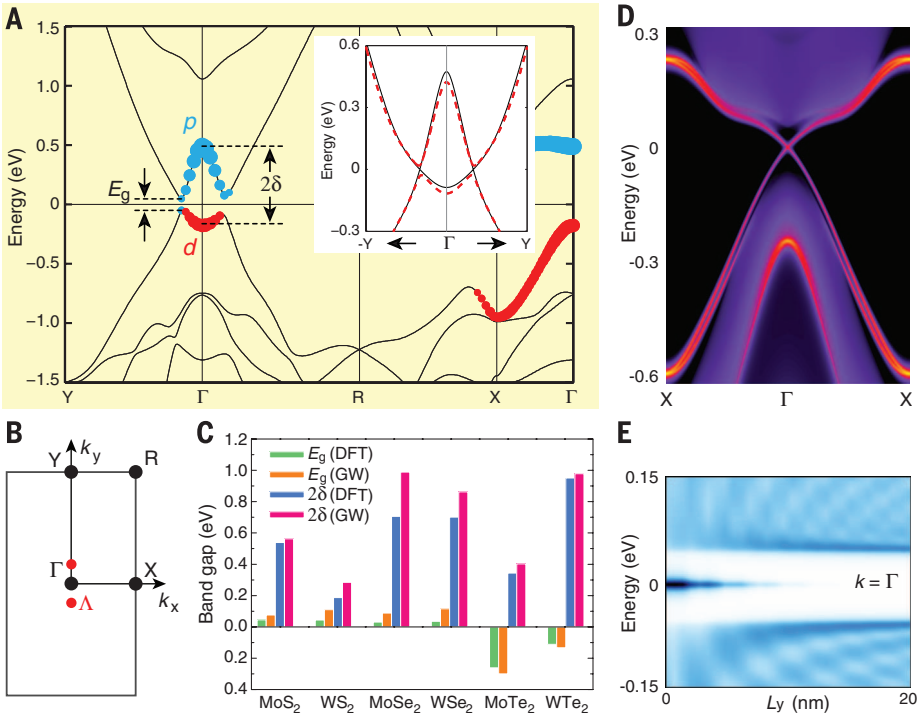

Fig. 2. Calculated electronic structures of 1T′-MX_2. (**A**) Band structure and (**B**) Brillouin zone of 1T′-MoS_2. E_g, fundamental gap; 2δ, inverted gap. The inset compares band structures with (red dashed line) and without (black solid line) spin-orbit coupling. Four time-reversal invariant momenta are marked by black dots and labeled as Γ, X, Y, and R. The locations of the fundamental gap are marked by red dots and labeled by Λ. (**C**) Fundamental gap (E_g) and inverted gap (2δ) of all six 1T′-MX_2. Detailed values are listed in table S1. (**D**) Edge density of states and (**E**) local density of states at Γ point as a function of distance away from the edge (L_y). A sharp peak from edge states appears in the gap with a decay length of ~5 nm.

Quantum spin Hall (QSH) insulators (*10*–*16*) have an insulating bulk but conducting edge states that are topologically protected from backscattering by time-reversal symmetry. Quantized conductance through QSH edge states have been experimentally demonstrated in HgTe/CdTe (*13*, *14*) and InAs/GaSb (*17*, *18*) quantum wells. This could in principle provide an alternative route to quantum electronic devices with low dissipation. However, the realization of such QSH-based devices for practical applications is impeded by three critical factors: (i) band gaps of existing QSH insulators are too small, which limits the operating regime to low temperatures. This has motivated efforts to search for large-gap QSH insulators (*19*–*26*); (ii) the small number of conducting channels (e^2/h per edge, where e is the elementary charge and h is Planck's constant) results in a small signal-to-noise ratio; and (iii) efficient methods of fast on/off switching are lacking.

Here, we use first-principles calculations to show that 2D materials can provide a practical platform for developing topological electronic devices that may potentially overcome the above hurdles. Specifically, we predict a class of large-gap (~0.1 eV) QSH insulators in 2D transition metal dichalcogenides (TMDCs) MX_2 with M = (W, Mo) and X = (Te, Se, S). We demonstrate the feasibility of a vdW-heterostructured topological field-effect transistor (vdW-TFET) made of 2D atomic layer materials. The proposed device exhibits a parametrically enhanced conductance through QSH edge channels in the "on" state and can be rapidly switched off via a topological phase transition by applying a vertical electric field. Our findings have potential applications in low-power quantum electronics and spintronics and may enable topological quantum computing based on Majorana fermions (*27*–*30*).

Monolayer TMDCs (*31*)—MX_2 with M = (W, Mo) and X = (Te, Se, S)—possess a variety of polytypic structures such as 1H, 1T, and 1T′ (*32*, *33*) shown in Fig. 1. The most-studied 1H structure is a sandwich of three planes of 2D hexagonally packed atoms, X-M-X, forming Bernal (ABA) stacking. In contrast, the three atomic planes in the 1T structure form rhombohedral (ABC) stacking. It has been known that the 1T structure in MX_2 is typically unstable in free-standing condition and undergoes a spontaneous lattice distortion in the x direction to form a period-doubling 2 × 1 distorted structure—i.e., the 1T′ structure, consisting of 1D zigzag chains along the y direction (Fig. 1C) (*33*); this structure is the subject of our work.

The electronic structures of various 1T′-MX_2 materials were obtained by many-body perturbation theory calculations (*34*). Figure 2A shows a typical band structure of 1T′-MX_2 using 1T′-MoS_2 as an example, and the results of the other five compounds are shown in fig. S1. Unlike its 1H or 1T counterparts, 1T′-MoS_2 is a semiconductor with a fundamental gap (E_g) of about 0.08 eV, located at $\Lambda = \pm(0, 0.146)\text{Å}^{-1}$

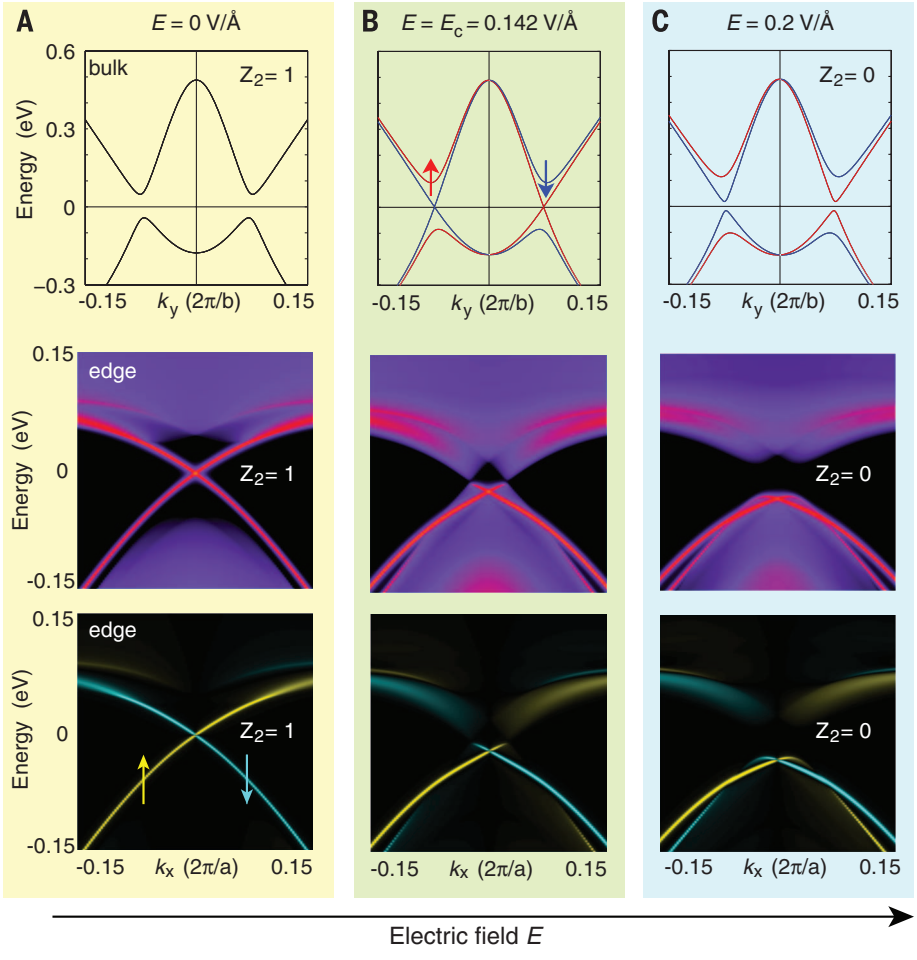

Fig. 3. Vertical electric field induced a topological phase transition. Shown are calculations for monolayer 1T′-MoS_2 under electric fields of (**A**) 0, (**B**) 0.142, and (**C**) 0.2 V/Å, respectively. The first, second, and third rows show the bulk band structure, edge density of states, and edge spin polarization, respectively.

(red dots in Fig. 2B). The conduction and valence bands display a camelback shape near Γ in the 2D Brillouin zone (BZ) (see Fig. 2B), suggestive of band inversion with a large inverted gap (2δ) at Γ of about 0.6 eV. The fundamental gap (E_g) and inverted gap (2δ) of all six 1T′-MX_2 are shown in Fig. 2C and listed in table S1. The inverted gap (2δ) was later used in the fitting of a low-energy $\boldsymbol{k} \cdot \boldsymbol{p}$ model (*34*). Because the 1T′ structure has inversion symmetry, we calculated the Z_2 index (0 or 1, indicating trivial or nontrivial topology, respectively) based on the parity criterion (*35*) of valence bands (fig. S2) and found Z_2 = 1, indicating that 2D 1T′-MX_2 materials are in the QSH insulator phase.

To understand the origin of the inverted band structure near Γ, we analyzed the orbital character of the bands and found that the valence band mainly consists of metal *d*-orbitals and the conduction band mainly consists of chalcogenide *p* orbitals, as expected. The unexpected band inversion arises from the period doubling of the metal chain in the 1T′ structure, which lowers the metal *d* orbital below chalcogenide *p* orbital (Fig. 2A) around Γ. The large band inversion at Γ (~0.6 eV) is an intrinsic characteristic of the 1T′ structure and already takes place without including spin-orbit interaction in the first-principles calculations. In the absence of spin-orbit coupling, this band inversion leads to the appearance of two Dirac cones centered at finite momenta on Y-Γ-Y in 2D BZ. Spin-orbit coupling then opens up a fundamental gap of 0.08 eV at the Dirac points (Fig. 2A, inset, and fig. S3), leading to a QSH insulator through a similar mechanism as the Kane-Mele model for graphene (*10*); we show that this is the case by using a low-energy $\boldsymbol{k} \cdot \boldsymbol{p}$ Hamiltonian (*34*) (fig. S4). In addition to MoS_2, we found that all other five 1T′-MX_2 have Z_2 nontrivial band topology.

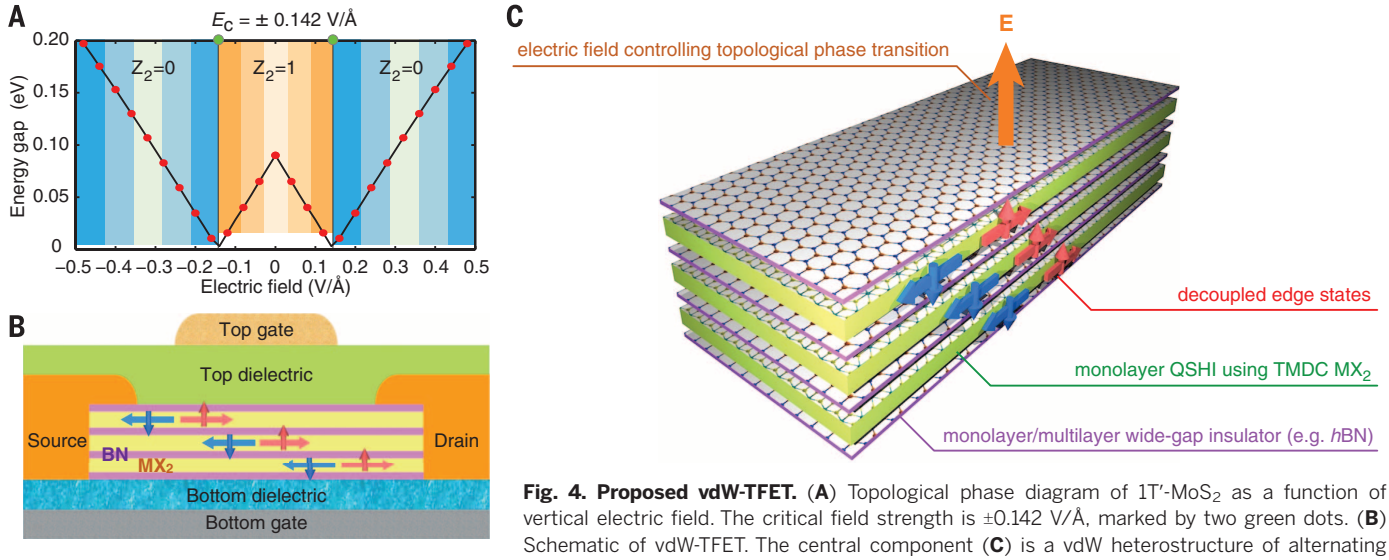

Fig. 4. Proposed vdW-TFET. (**A**) Topological phase diagram of 1T′-MoS_2 as a function of vertical electric field. The critical field strength is ±0.142 V/Å, marked by two green dots. (**B**) Schematic of vdW-TFET. The central component (**C**) is a vdW heterostructure of alternating monolayer 1T′-MX_2 and mono-/multilayer wide-gap insulators such as hBN, with horizontal width as narrow as ~20 nm. Carriers (charge or spin) are injected from the source electrode and ejected into the drain electrode. On/off switch is controlled by vertical electric field through the top and bottom gates. Mono-/multilayer wide-gap insulators effectively screen the interaction between adjacent MX_2 layers, preventing them from detrimental topological phase change and parametrically increasing the number of edge channels.

The QSH insulator phase in 2D 1T′-MX_2 leads to helical edge states that are protected from localization and elastic backscattering by time-reversal symmetry. Figure 2D displays the edge states of 1T′-MoS_2 obtained from surface Green's function calculations (*34*), showing a pair of counter-propagating edge modes with a high velocity of ~1.0×10^5 m/s that cross at Γ and carry opposite spin polarizations. From the local density of states in Fig. 2E, we find the decay length of these helical edge states to be as short as 5 nm. The short localization length can greatly reduce scattering with bulk states (*36*), hence increasing the transport lifetime. Similar results were found for five other TMDCs (figs. S5 and S6).

The inverted bands between chalcogenide's *p* and metal's *d* orbitals located on well-separated planes offer a facile mechanism to control topological electronic properties by electric field, which is highly desirable for vdW devices. Based on first-principles calculations, we found that a vertical electric field indeed induces a topological phase transition in 1T′-MX_2, as shown in Fig. 3 for 1T′-MoS_2. Here, the electric field breaks inversion symmetry and introduces a strong Rashba splitting of the doubly degenerate bands near the fundamental gap E_g at the Λ points. As the field increases, E_g first decreases to zero at a critical field strength of 0.142 V/Å and then reopens (see Fig. 4A). This gap-closing transition induces a topology change to a trivial phase (*11*, *37*), leading to the destruction of helical edge states.

The above findings point to the possibility of an all-electrical control of the on/off charge/spin conductance of helical edge states, which would have substantial implications for QSH-based devices (*38*–*43*). Here, we propose a TFET based on vdW heterostructures of 2D TMDCs and 2D wide-gap insulators. The proposed device is sketched in Fig. 4B, where the top and bottom gates supply the vertical electric field to control the on/off function. Two-dimensional wide-gap insulators such as hexagonal boron nitride (hBN) (*44*) electrically insulate adjacent QSH layers, hence protecting parallel helical edge channels from being gapped by interlayer hybridization. This can parametrically increase the number of edge transport channels. Under ideal conditions, this device will support dissipationless charge/spin transport in the "on" state (Z_2 = 1), with a quantized conductance of $2Ne^2/h$, where N is the number of QSH layers. Applying a moderate electric field will transform 1T′-MX_2 into an ordinary insulator (Z_2 = 0) and turn the edge conduction off (Fig. 4A).

The proposed vdW-TFET may possess important technical advantages, thanks to an operation mechanism that is fundamentally different from traditional metal-oxide-semiconductor FETs (MOS-FET). MOS-FET works by injecting/depleting free carrier beneath the gate, with a resistor–capacitor-type response time influenced by carrier concentration and mobility in the working channel, whereas our vdW-TFET works by switching the presence/absence of topologically protected conduction channels. The electric field–induced topological phase transition can happen very rapidly, with an electronic response time scale (*45*, *46*). In addition, the vdW heterostructure and the 2D nature of vdW-TFET make it convenient to both vertically and horizontally pattern devices at a large scale. The short decay length of helical edge states allows the minimum horizontal feature size of vdW-TFET to be ~20 nm, enabling high device density on a chip. Horizontally patterned TFET devices of such nanoscale size have large edge-to-area ratios, which will greatly reduce the contribution of thermally populated bulk carriers to the total electric current and hence enhance the on/off ratio. The predicted QSH insulators and their vdW heterostructures may provide a platform for realizing low-dissipation quantum electronics and spintronics (*38*–*43*).

From a materials perspective, the 1T′ structure in monolayer MoS_2 has recently been observed in high-resolution transmission electron microscopy experiments (*33*). We have checked the structural stability of 1T′ by carrying out first-principles calculations (fig. S7). Although MoS_2, $MoSe_2$, $MoTe_2$, WS_2, and WSe_2 are more stable in the 1H structure, we find that there exists a large energy barrier of more than 1 eV/MX_2 between 1T′ and 1H for all MX_2, suggesting that the 1T′ structure can be stabilized under appropriate chemical (*47*), thermal, or mechanical conditions. Moreover, we found that the 1T structure is unstable and will spontaneously relax to 1T′, like in a Peierls distortion. We also verified the stability of the 1T′ structure by computing its phonon dispersion (fig. S8). The absence of imaginary frequencies throughout the 2D BZ provides direct evidence of the structural stability in all 1T′-MX_2.

Encouragingly, the desired 1T′ structure with intrinsic band inversion is the natural ground-state structure of WTe_2 (*31*), also confirmed by our stability calculation. Although monolayer WTe_2 was found to be a semimetal from our calculation, the small negative fundamental gap can be easily lifted by a tensile strain as small as ~1% (fig. S9). We also found that hBN used as a dielectric in the aforementioned vdW-TFET device has little effect on the electronic structure of 1T′-WTe_2 near the Fermi level (fig. S10). These attractive features make WTe_2 potentially the most promising 2D TMDC for realizing the QSH effect and related vdW devices.

REFERENCES AND NOTES

1. K. S. Novoselov *et al*., *Science* **306**, 666–669 (2004).
2. K. S. Novoselov *et al*., *Proc. Natl. Acad. Sci. U.S.A.* **102**, 10451–10453 (2005).
3. C. Lee, X. Wei, J. W. Kysar, J. Hone, *Science* **321**, 385–388 (2008).
4. A. H. Castro Neto, F. Guinea, N. M. R. Peres, K. S. Novoselov, A. K. Geim, *Rev. Mod. Phys.* **81**, 109–162 (2009).
5. K. F. Mak, C. Lee, J. Hone, J. Shan, T. F. Heinz, *Phys. Rev. Lett.* **105**, 136805 (2010).
6. Q. H. Wang, K. Kalantar-Zadeh, A. Kis, J. N. Coleman, M. S. Strano, *Nat. Nanotechnol.* **7**, 699–712 (2012).
7. J. Feng, X. Qian, C.-W. Huang, J. Li, *Nat. Photonics* **6**, 866–872 (2012).
8. K. S. Kim *et al*., *Nature* **457**, 706–710 (2009).
9. A. K. Geim, I. V. Grigorieva, *Nature* **499**, 419–425 (2013).
10. C. L. Kane, E. J. Mele, *Phys. Rev. Lett.* **95**, 226801 (2005).
11. C. L. Kane, E. J. Mele, *Phys. Rev. Lett.* **95**, 146802 (2005).
12. B. A. Bernevig, S.-C. Zhang, *Phys. Rev. Lett.* **96**, 106802 (2006).
13. B. A. Bernevig, T. L. Hughes, S.-C. Zhang, *Science* **314**, 1757–1761 (2006).
14. M. König *et al*., *Science* **318**, 766–770 (2007).
15. M. Z. Hasan, C. L. Kane, *Rev. Mod. Phys.* **82**, 3045–3067 (2010).
16. X.-L. Qi, S.-C. Zhang, *Rev. Mod. Phys.* **83**, 1057–1110 (2011).
17. C. Liu, T. L. Hughes, X.-L. Qi, K. Wang, S.-C. Zhang, *Phys. Rev. Lett.* **100**, 236601 (2008).
18. L. Du, I. Knez, G. Sullivan, R.-R. Du, http://arxiv.org/abs/1306.1925 (2013).
19. S. Murakami, *Phys. Rev. Lett.* **97**, 236805 (2006).
20. C.-C. Liu, W. Feng, Y. Yao, *Phys. Rev. Lett.* **107**, 076802 (2011).
21. D. Xiao, W. Zhu, Y. Ran, N. Nagaosa, S. Okamoto, *Nat. Commun.* **2**, 596–596 (2011).
22. Y. Xu *et al*., *Phys. Rev. Lett.* **111**, 136804 (2013).
23. H. Weng, X. Dai, Z. Fang, *Phys. Rev. X* **4**, 011002 (2014).
24. M. A. Cazalilla, H. Ochoa, F. Guinea, *Phys. Rev. Lett.* **113**, 077201 (2014).
25. D. Kong, Y. Cui, *Nat. Chem.* **3**, 845–849 (2011).
26. K. Yang, W. Setyawan, S. Wang, M. Buongiorno Nardelli, S. Curtarolo, *Nat. Mater.* **11**, 614–619 (2012).
27. L. Fu, C. L. Kane, *Phys. Rev. Lett.* **100**, 096407 (2008).
28. L. Fu, C. L. Kane, *Phys. Rev. B* **79**, 161408 (2009).
29. J. Alicea, *Rep. Prog. Phys.* **75**, 076501 (2012).
30. S. Mi, D. I. Pikulin, M. Wimmer, C. W. J. Beenakker, *Phys. Rev. B* **87**, 241405 (2013).
31. J. A. Wilson, A. D. Yoffe, *Adv. Phys.* **18**, 193–335 (1969).
32. J. Heising, M. G. Kanatzidis, *J. Am. Chem. Soc.* **121**, 11720–11732 (1999).
33. G. Eda *et al*., *ACS Nano* **6**, 7311–7317 (2012).
34. Supplementary materials are available on *Science* Online.
35. L. Fu, C. L. Kane, *Phys. Rev. B* **76**, 045302 (2007).
36. J. I. Väyrynen, M. Goldstein, L. I. Glazman, *Phys. Rev. Lett.* **110**, 216402 (2013).
37. S. Murakami, *New J. Phys.* **9**, 356 (2007).
38. J. Wunderlich *et al*., *Science* **330**, 1801–1804 (2010).
39. D. Pesin, A. H. MacDonald, *Nat. Mater.* **11**, 409–416 (2012).
40. F. Mahfouzi, N. Nagaosa, B. K. Nikolić, *Phys. Rev. Lett.* **109**, 166602 (2012).
41. C. Brüne *et al*., *Nat. Phys.* **8**, 485–490 (2012).
42. C. H. Li *et al*., *Nat. Nanotechnol.* **9**, 218–224 (2014).
43. A. R. Mellnik *et al*., *Nature* **511**, 449–451 (2014).
44. C. R. Dean *et al*., *Nat. Nanotechnol.* **5**, 722–726 (2010).
45. J. Liu *et al*., *Nat. Mater.* **13**, 178–183 (2014).
46. P. Michetti, B. Trauzettel, *Appl. Phys. Lett.* **102**, 063503 (2013).
47. M. Calandra, *Phys. Rev. B* **88**, 245428 (2013).

ACKNOWLEDGMENTS

We acknowledge support from NSF under award DMR-1120901 (X.Q. and J.L.), U.S. Department of Energy, Office of Basic Energy Sciences, Division of Materials Sciences and Engineering under award DE-SC0010526 (L.F.), and the Science and Technology Center on Integrated Quantum Materials, NSF grant no. DMR-1231319 (J.W.L.). Computational time on the Extreme Science and Engineering Discovery Environment (XSEDE) under grant nos. TG-DMR130038 and TG-DMR140003 is gratefully acknowledged. X.Q. and J.W.L. contributed equally to this work. MIT has applied for a provisional patent based on the content of this paper. Both atomic and electronic structures of 1T′-MX_2 can be found in the supplementary materials.

SUPPLEMENTARY MATERIALS

www.sciencemag.org/content/346/6215/1344/suppl/DC1
Supplementary Methods
Figs. S1 to S10
Tables S1 and S2
References (*48*–*62*)

2 June 2014; accepted 5 November 2014
10.1126/science.1256815

Quantum spin Hall effect in two-dimensional transition metal dichalcogenides

Xiaofeng Qian *et al.*

Science **346**, 1344 (2014);
DOI: 10.1126/science.1256815

Science (print ISSN 0036-8075; online ISSN 1095-9203) is published weekly, except the last week in December, by the American Association for the Advancement of Science, 1200 New York Avenue NW, Washington, DC 20005.

www.sciencemag.org/cgi/content/full/science.1256815/DC1

Supplementary Materials for

Quantum spin Hall effect in two-dimensional transition metal dichalcogenides

Xiaofeng Qian, Junwei Liu, Liang Fu,* Ju Li *

*Corresponding author. E-mail: liangfu@mit.edu (L.F.); liju@mit.edu (J.L.)

Published 20 November 2014 on *Science* Express
DOI: 10.1126/science.1256815

This PDF file includes:

Methods

S1. Ground-state atomic structures of monolayer transition metal dichalcogenides 1T'-MX_2

Ground-state atomic structures of all six monolayer transition metal dichalcogenides 1T'-MX_2 were fully relaxed using first-principles density functional theory (DFT) (*48, 49*). The calculations were performed by the Vienna Ab initio Simulation Package (VASP) (*50, 51*) with projector-augmented wave method (*52*) and exchange-correlation functional in the Perdew-Berke-Ernzerhof's form (*53*) within the generalized-gradient approximation (*54, 55*). We used an energy cutoff of 400 eV and maximum residual force less than 0.001 eV/Å. The Monkhorst-Pack $\boldsymbol{k}$-point sampling (*56*) of $8\times8\times1$ was adopted for the Brillouin zone integration, and a large vacuum region of more than 16 Å was applied to the plane normal direction in order to minimize image interactions from the periodic boundary condition. Moreover, phonon dispersion curves were calculated by first-principles density-functional perturbation theory and the results are shown in Fig. S8 for all six materials.

S2. Bulk electronic structure of monolayer transition metal dichalcogenides 1T'-MX_2

We first computed the electronic band structures of monolayer transition metal dichalcogenides 1T'-MX_2 using first-principles DFT. Since the calculated DFT band structures only provide qualitative electronic structure for quasi-particles such as electrons and holes, we further computed quasi-particle band structures using more accurate method, namely, many-body perturbation theory within Hedin's G_0W_0 approximation (*57, 58*). The results are shown in Fig. 2A for monolayer 1T'-MoS_2 and Fig. S1 for all six materials. Fundamental gap (E_g) and inverted gap (2δ) of monolayer transition metal dichalcogenides 1T'-MX_2 are collected in Table S1 and Fig. 2C.

S3. Electronic structure of edge states in monolayer transition metal dichalcogenides 1T'-MX_2

The Z_2 trivial/nontrivial band topology has distinct consequence on the helical edge state. To reveal the helical edge states of monolayer 1T'-MX_2 explicitly, we performed iterative Green's function calculations (*59*) using tight-binding Hamiltonian (*60, 61*) constructed from many-body perturbation theory with the GW approximation (*57, 58*), where we extracted the edge density of states, spin polarization, and decay length of the helical edge states. The results are shown in Fig. 3 for monolayer 1T'-MoS_2 and Fig. S5 and Fig. S6 for all six materials. Furthermore, to investigate the effect of vertical electric field on the electronic structure of monolayer 1T'-MoS_2 QSHI, we introduce a corresponding change in the diagonal elements of first-principles tight-binding Hamiltonian. This approach is validated by comparing with direct self-consistent first-principles calculations under the same electric field. In addition, we found the electric field has negligible impact on ionic positions.

S4. Z_2 invariant of monolayer transition metal dichalcogenides 1T'-MX_2

The Z_2 invariant was obtained by explicitly calculating band parity of the materials with inversion symmetry (*35*). The results are shown in Fig. S2 for all six materials with inversion center located at the middle of the bond formed by two transition metal atoms in the quasi-one dimensional chain along y direction. We also cross-checked all the results by the *n*-field method (*62*).

S5. $\mathbf{k}\cdot\mathbf{p}$ model for monolayer transition metal dichalcogenides 1T'-MX_2

The valence band mainly consists of *d*-orbitals of M atoms, while the conduction band mainly consists of p_y-orbitals of X atoms. The origin of such inversion roots in the formation of quasi-one dimensional transition metal chains in the 1T' structure, which lowers M's *d* orbital below p X's *p* to with respect to the original 1T structure, leading to the band inversion at Γ point (Fig. S3). By analyzing the symmetry properties of these bands, we develop a low-energy $\mathrm{k}\cdot\mathrm{p}$ Hamiltonian for 1T'-MX_2,

$$H = \begin{pmatrix} E_p(k_x,k_y) & 0 & -iv_1\hbar k_x & v_2\hbar k_y \\ 0 & E_p(k_x,k_y) & v_2\hbar k_y & -iv_1\hbar k_x \\ iv_1\hbar k_x & v_2\hbar k_y & E_d(k_x,k_y) & 0 \\ v_2\hbar k_y & iv_1\hbar k_x & 0 & E_d(k_x,k_y) \end{pmatrix},$$

where $E_p = -\delta - \frac{\hbar^2 k_x^2}{2m_x^p} - \frac{\hbar^2 k_y^2}{2m_y^p}$, and $\mathrm{E_d} = \delta + \frac{\hbar^2 \mathrm{k_x^2}}{2\mathrm{m_x^d}} + \frac{\hbar^2 \mathrm{k_y^2}}{2\mathrm{m_y^d}}$. Here $\delta < 0$ corresponds to the *d-p* band inversion. By fitting with first-principles band structure in Fig. 2A, we obtain the parameters: $\delta = -0.33$ eV, $v_1 = 3.87\times10^5$ m/s, $v_2 = 0.46\times10^5$ m/s, $m_x^p = 0.50\, m_\mathrm{e}$, $m_y^p = 0.16\, m_\mathrm{e}$, $m_x^d = 2.48\, m_\mathrm{e}$, and $m_y^d = 0.37\, m_\mathrm{e}$, where m_e is the free electron mass. Fig. S4 shows the comparison of band structures obtained from first-principles GW calculations and the $\mathrm{k}\cdot\mathrm{p}$ model.

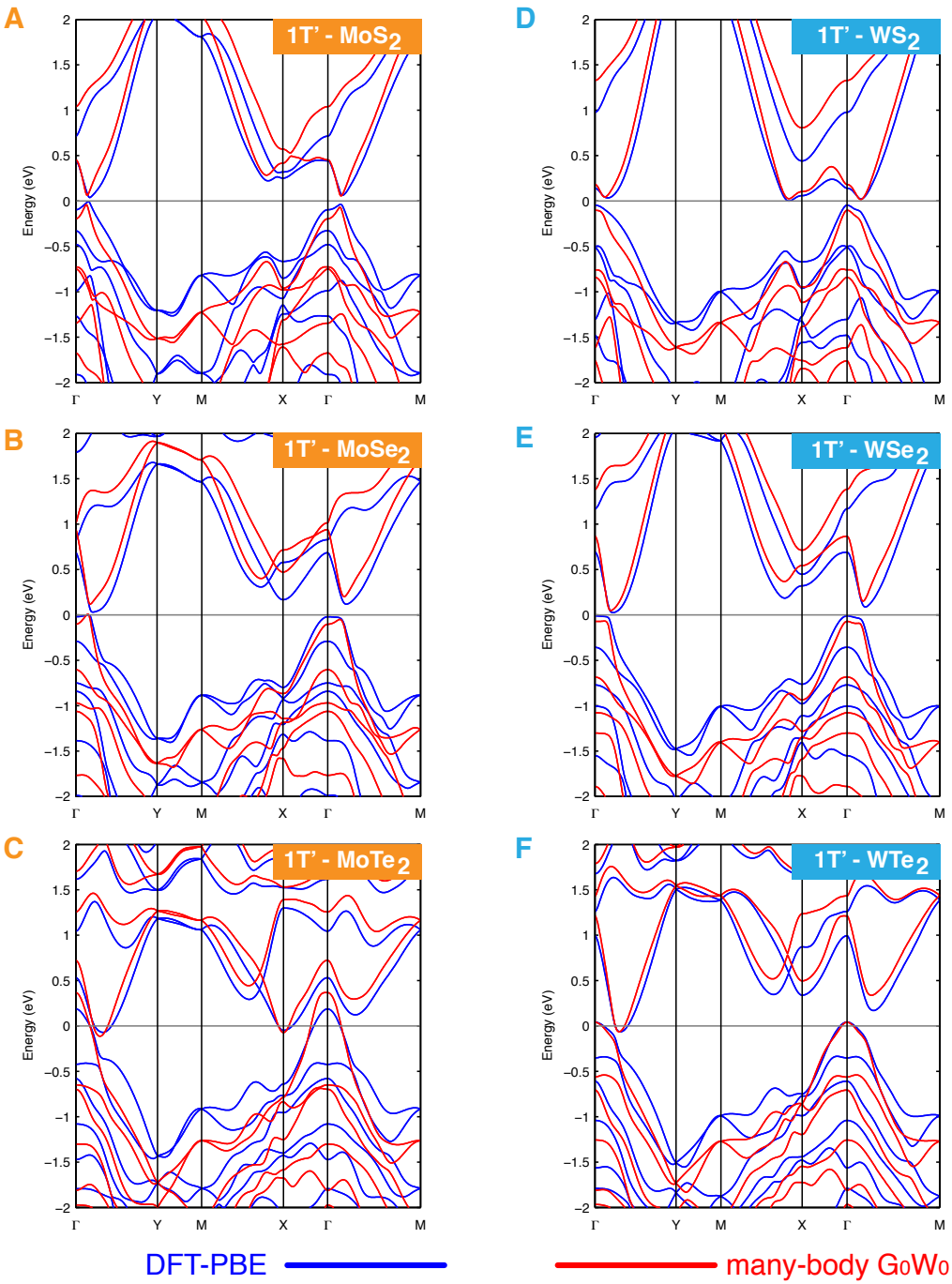

Fig. S1.
Electronic band structure of monolayer transition metal dichalcogenides 1T'-MX_2. Blue lines stand for first-principles density-functional theory calculations. Red lines stand for many-body G_0W_0 theory calculations.

A 1T' - MoS_2

Γ_i	parity ξ_{2m} of occupied bands	$\delta_i = \prod_m \xi_{2m}$
Γ	+ − − + − + + − − + + −	+
X	− + + − + − − + + − − +	−
Y	+ − + − + − + − + − + −	−
R	+ − + − + − + − + − + −	−
	Z_2 invariant ν: $(-1)^\nu = \prod_i \delta_i$	ν = 1

B 1T' - $MoSe_2$

Γ_i	parity ξ_{2m} of occupied bands	$\delta_i = \prod_m \xi_{2m}$
Γ	+ − + − − + − + + − + − +	+
X	− + + − + − + − − + − + −	−
Y	+ − + − + − + + − − + − +	−
R	− + + + − + − − + + − − +	−
	Z_2 invariant ν: $(-1)^\nu = \prod_i \delta_i$	ν = 1

C 1T' - $MoTe_2$

Γ_i	parity ξ_{2m} of occupied bands	$\delta_i = \prod_m \xi_{2m}$
Γ	+ − + − − + − + − + − + +	+
X	− + + − + − + − + − + − −	−
Y	+ − + − + − + − + − + − −	−
R	+ − + − + − + − + − + − +	−
	Z_2 invariant ν: $(-1)^\nu = \prod_i \delta_i$	ν = 1

D 1T' - WS_2

Γ_i	parity ξ_{2m} of occupied bands	$\delta_i = \prod_m \xi_{2m}$
Γ	+ − − + − + + − − + − + +	+
X	+ − + − − + − + + − − + −	−
Y	− + + − + − − + − + + − −	−
R	− + + + − + − + − + − + +	−
	Z_2 invariant ν: $(-1)^\nu = \prod_i \delta_i$	ν = 1

E 1T' - WSe_2

Γ_i	parity ξ_{2m} of occupied bands	$\delta_i = \prod_m \xi_{2m}$
Γ	+ − + − − + − + + − + − +	+
X	− + + − + − + − − + − + −	−
Y	− + + − + − + + − − + + −	−
R	− + + − + − + − + − + + −	−
	Z_2 invariant ν: $(-1)^\nu = \prod_i \delta_i$	ν = 1

F 1T' - WTe_2

Γ_i	parity ξ_{2m} of occupied bands	$\delta_i = \prod_m \xi_{2m}$
Γ	+ − + − − + − + − + − + +	+
X	− + + − + − + − + − + − −	−
Y	− + + − + − + + − − + − +	−
R	− + + + − − + + − − + + −	−
	Z_2 invariant ν: $(-1)^\nu = \prod_i \delta_i$	ν = 1

Fig. S2.
Parity tables for monolayer transition metal dichalcogenides 1T'-MX_2 at time-reversal invariant momenta, and the corresponding Z_2 invariants, ν. All Z_2 invariants are 1, indicating all six 1T'-MX_2 are topologically nontrivial. We choose the inversion center at the middle of the short M-M bond formed by two transition metal atoms.

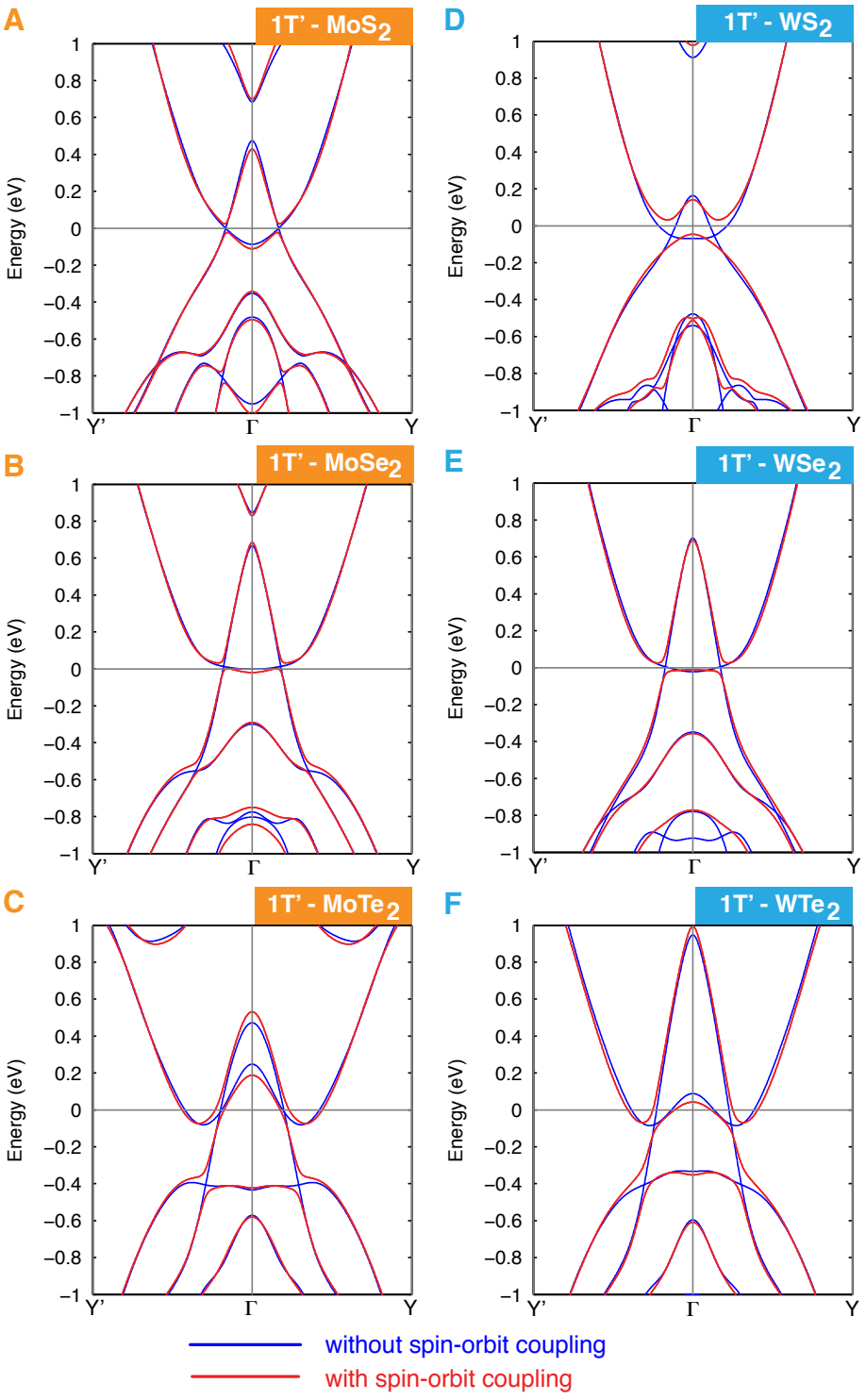

Fig. S3.
Electronic band structure of monolayer transition metal dichalcogenides 1T'-MX_2 with and without spin-orbit coupling. The calculations were performed by first-principles density-functional theory with the PBE exchange-correlation functional.

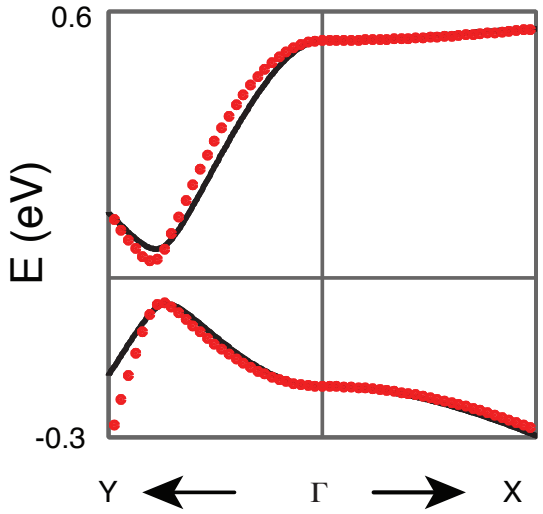

Fig. S4.
Comparison of band structures obtained from first-principles GW calculation (black line) and the fitted k · p Hamiltonian (red dots) for 1T'-MoS_2.

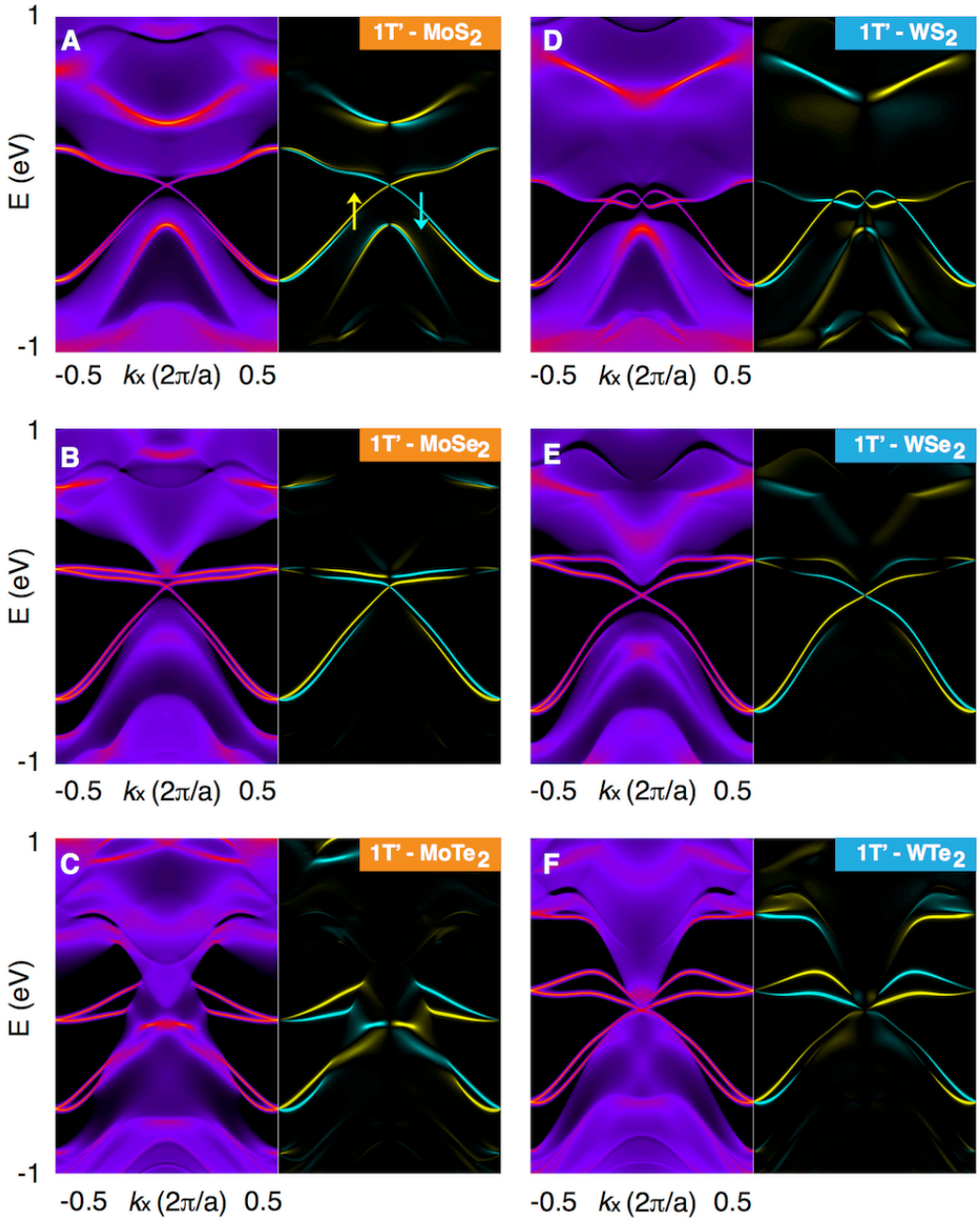

Fig. S5.
Electronic structure of helical edge states in monolayer transition metal dichalcogenides 1T'-MX_2. For each MX_2, the left subpanel shows the density of states while the right subpanel shows the corresponding spin polarization. These helical edge states are a manifestation of nontrivial topology of monolayer 1T'-MX_2.

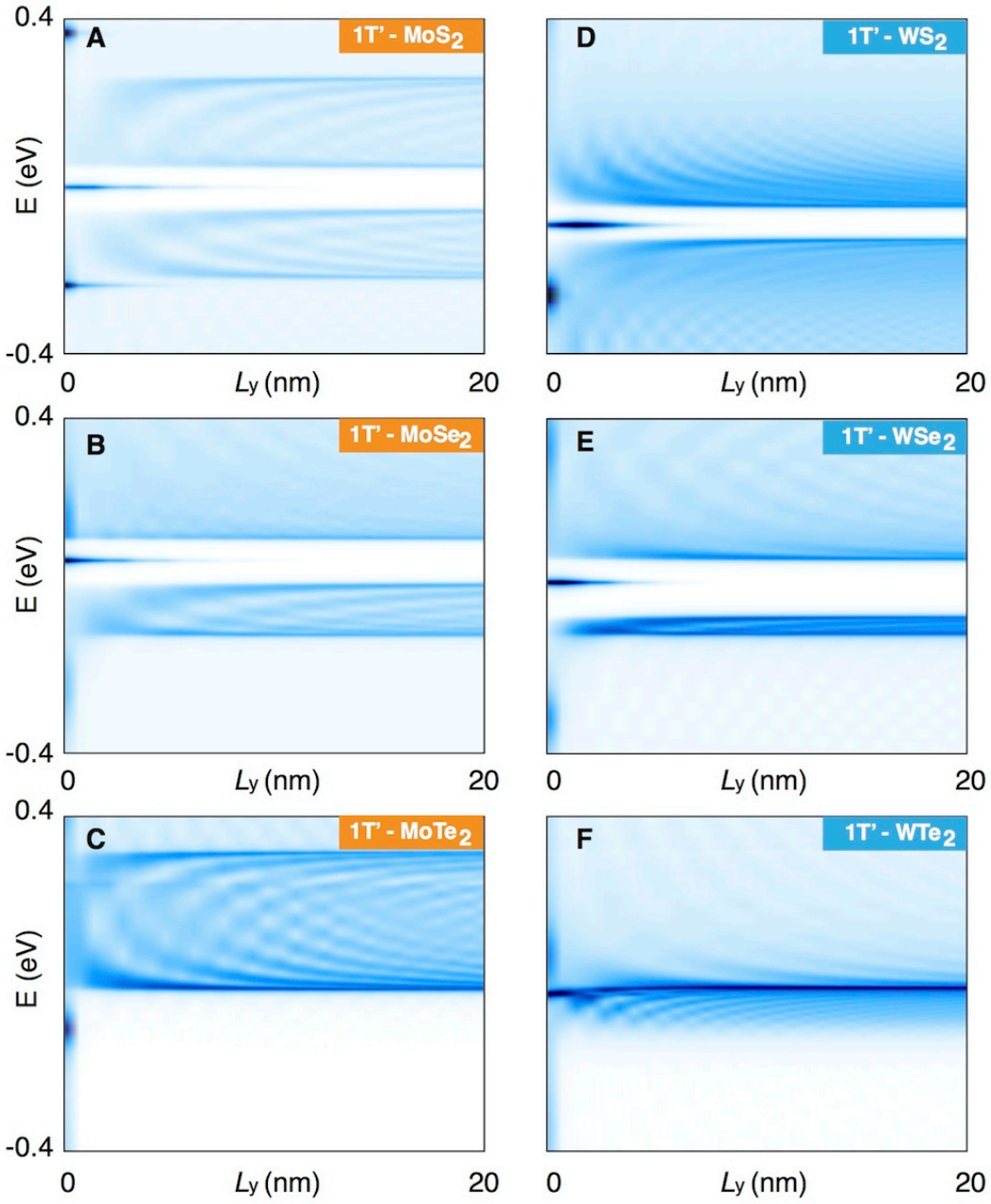

Fig. S6.
Local density of states as function of penetration depth away from the edge at L_y=0 in monolayer transition metal dichalcogenide 1T'-MX_2. Due to the semi-metallic nature of 1T'-$MoTe_2$ and 1T'-WTe_2, local density of states from edge and bulk are entangled with each other. Therefore, the decay lengths of their edge states are not accessible.

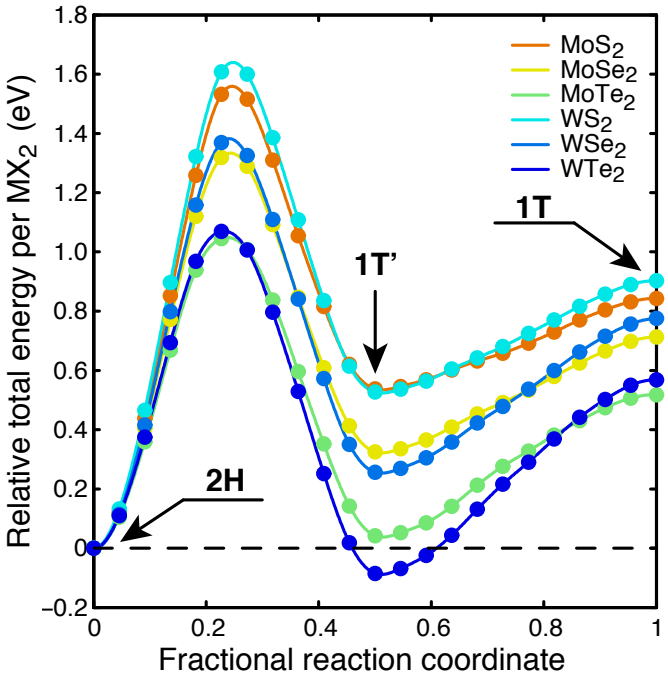

Fig. S7.
Structural stability of monolayer transition metal dichalcogenide 1T'-MX_2: relative total energy per MX_2 as a function of fractional reaction coordinate.

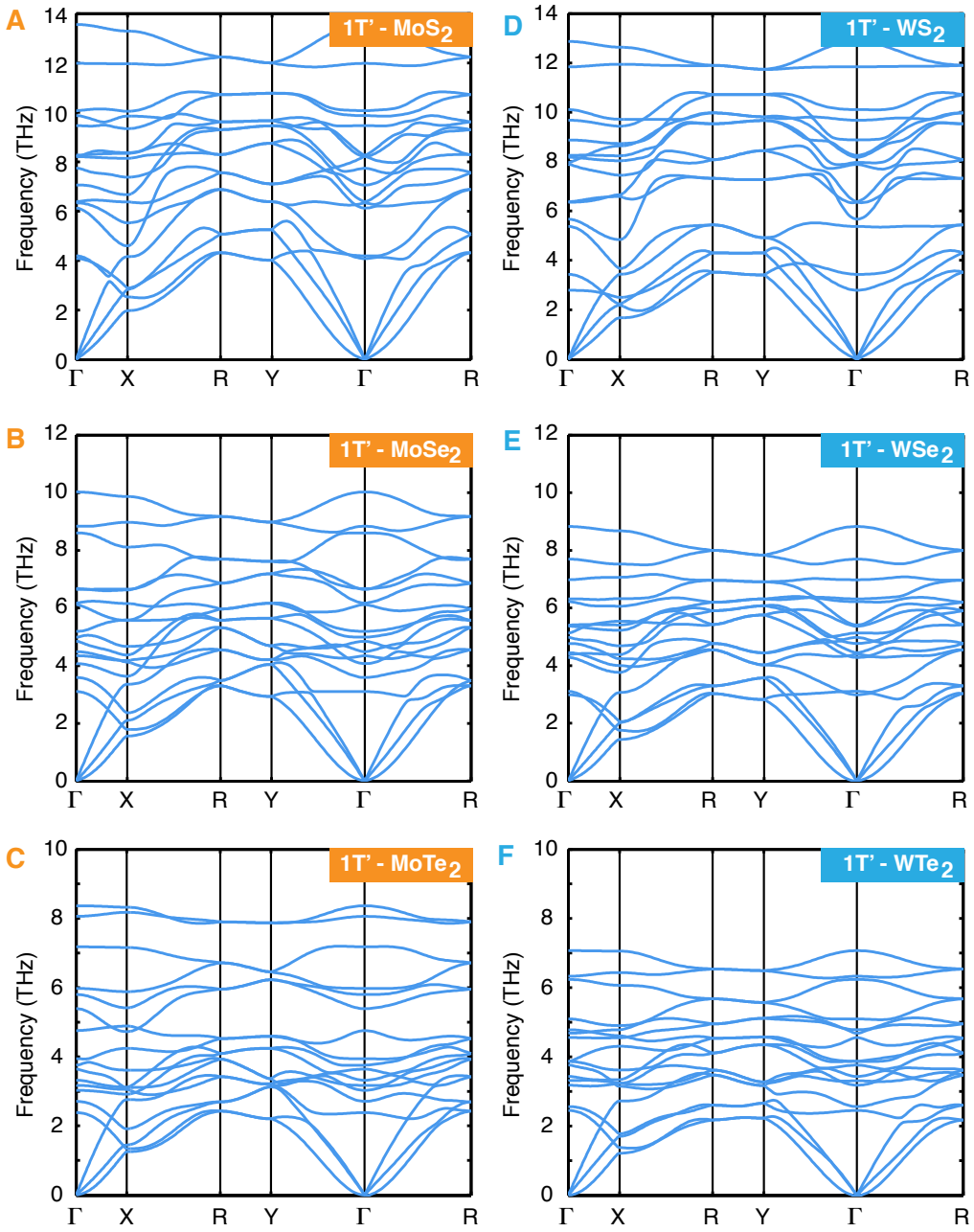

Fig. S8.
Phonon dispersion curves of monolayer transition metal dichalcogenide 1T'-MX_2. The absence of imaginary frequency demonstrates the structural stability of all six monolayer 1T'-MX_2.

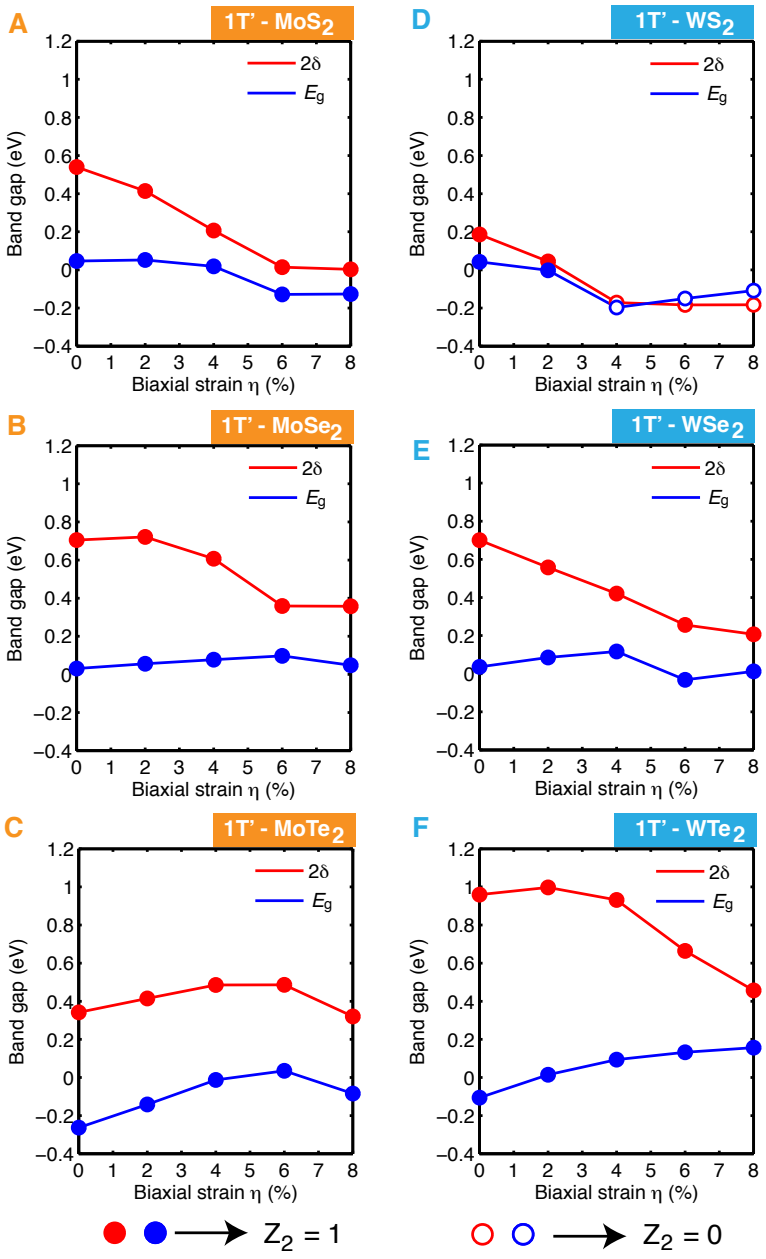

Fig. S9.
Effect of biaxial strain on fundamental gap (E_g), inverted gap (2δ), and Z_2 invariant of 1T'-MX_2. Positive inverted gap (2δ) indicates Z_2=1 and positive E_g indicates insulator.

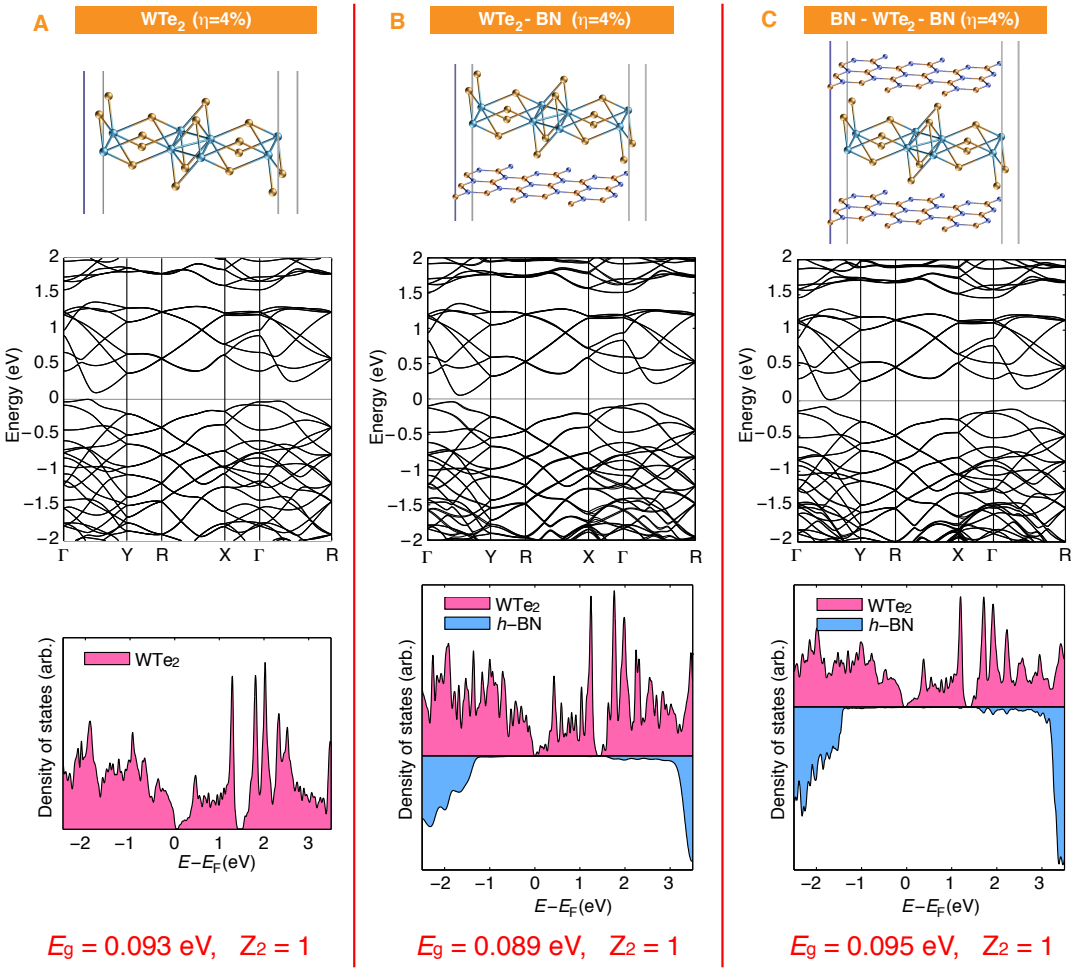

Fig. S10.
Effect of van der Waals heterostacking with hexagonal BN monolayers on electronic structure, projected density of states, fundamental band gap (E_g), and Z_2 invariant of 1T'-WTe_2 under 4% biaxial strain. The supercell was constructed by 2x2 1T'-WTe_2 and $3\sqrt{3}\times3$ BN monolayers under 4% biaxial strain to minimize the lattice mismatch for first-principles calculations. (**A**) biaxially-strained monolayer 1T'-WTe_2. (**B**) strained 1T'-WTe_2 stacked on hexagonal BN monolayer. (**C**) strained 1T'-WTe_2 sandwiched by two hexagonal BN layers. It clearly shows that BN monolayers have negligible effect on the electronic structure of 1T'-WTe_2 in a wide energy range around the Fermi level, demonstrating hexagonal BN sheets as ideal dielectric layers for the experimental realization of van der Waals heterostructure-based topological field effect transistor.

1T' phase	Fundamental gap (E_g, eV)		Inverted gap (2δ, eV)	
	DFT-PBE	G_0W_0	DFT-PBE	G_0W_0
WTe_2	-0.112	-0.133	0.952	0.978
$MoTe_2$	-0.262	-0.300	0.344	0.403
WSe_2	0.036	0.116	0.701	0.863
$MoSe_2$	0.031	0.088	0.706	0.988
WS_2	0.044	0.110	0.187	0.284
MoS_2	0.045	0.076	0.540	0.562

Table S1.
Fundamental gap (E_g) and inverted gap (2δ) of monolayer transition metal dichalcogenides 1T'-MX_2 calculated by first-principles density-functional theory with PBE exchange-correlation functional and many-body perturbation theory within the G_0W_0 approximation.

WTe2 1.0 6.314769 0.000000 0.000000 0.000000 3.492485 0.000000 0.000000 0.000000 20.160000 W Te 2 4 Selective dynamics Direct 0.821873 0.750000 0.495163 T T T 0.178127 0.250000 0.504838 T T T 0.081802 0.750000 0.603508 T T T 0.572013 0.250000 0.573093 T T T 0.427987 0.750000 0.426907 T T T 0.918198 0.250000 0.396492 T T T	MoTe2 1.0 6.382718 0.000000 0.000000 0.000000 3.450605 0.000000 0.000000 0.000000 20.160000 Mo Te 2 4 Selective dynamics Direct 0.818044 0.750000 0.495460 T T T 0.181956 0.250000 0.504540 T T T 0.077746 0.750000 0.602203 T T T 0.569509 0.250000 0.573108 T T T 0.430491 0.750000 0.426892 T T T 0.922254 0.250000 0.397797 T T T
WSe2 1.0 5.944039 0.000000 0.000000 0.000000 3.301128 0.000000 0.000000 0.000000 20.160000 W Se 2 4 Selective dynamics Direct 0.810843 0.750000 0.495938 T T T 0.189157 0.250000 0.504062 T T T 0.084550 0.750000 0.593738 T T T 0.577032 0.250000 0.569474 T T T 0.422968 0.750000 0.430526 T T T 0.915450 0.250000 0.406262 T T T	MoSe2 1.0 5.964753 0.000000 0.000000 0.000000 3.281478 0.000000 0.000000 0.000000 20.160000 Mo Se 2 4 Selective dynamics Direct 0.809643 0.750000 0.496007 T T T 0.190357 0.250000 0.503993 T T T 0.082606 0.750000 0.592887 T T T 0.575259 0.250000 0.569562 T T T 0.424741 0.750000 0.430438 T T T 0.917394 0.250000 0.407113 T T T
WS2 1.0 5.711630 0.000000 0.000000 0.000000 3.191390 0.000000 0.000000 0.000000 20.160000 W S 2 4 Selective dynamics Direct 0.802593 0.750000 0.496539 T T T 0.197407 0.250000 0.503461 T T T 0.086405 0.750000 0.586678 T T T 0.579854 0.250000 0.565748 T T T 0.420146 0.750000 0.434252 T T T 0.913595 0.250000 0.413322 T T T	MoS2 1.0 5.722851 0.000000 0.000000 0.000000 3.173255 0.000000 0.000000 0.000000 20.160000 Mo S 2 4 Selective dynamics Direct 0.802497 0.750000 0.496310 T T T 0.197503 0.250000 0.503690 T T T 0.083583 0.750000 0.586158 T T T 0.578635 0.250000 0.565937 T T T 0.421365 0.750000 0.434063 T T T 0.916417 0.250000 0.413842 T T T

Table S2.
Relaxed atomic structures of 1T'-MX_2 in the VASP/POSCAR format.

References

1. K. S. Novoselov, A. K. Geim, S. V. Morozov, D. Jiang, Y. Zhang, S. V. Dubonos, I. V. Grigorieva, A. A. Firsov, Electric field effect in atomically thin carbon films. *Science* **306**, 666–669 (2004). Medline doi:10.1126/science.1102896

2. K. S. Novoselov, D. Jiang, F. Schedin, T. J. Booth, V. V. Khotkevich, S. V. Morozov, A. K. Geim, Two-dimensional atomic crystals. *Proc. Natl. Acad. Sci. U.S.A.* **102**, 10451–10453 (2005). Medline doi:10.1073/pnas.0502848102

3. C. Lee, X. Wei, J. W. Kysar, J. Hone, Measurement of the elastic properties and intrinsic strength of monolayer graphene. *Science* **321**, 385–388 (2008). Medline doi:10.1126/science.1157996

4. A. H. Castro Neto, F. Guinea, N. M. R. Peres, K. S. Novoselov, A. K. Geim, The electronic properties of graphene. *Rev. Mod. Phys.* **81**, 109–162 (2009). doi:10.1103/RevModPhys.81.109

5. K. F. Mak, C. Lee, J. Hone, J. Shan, T. F. Heinz, Atomically thin MoS_2: A new direct-gap semiconductor. *Phys. Rev. Lett.* **105**, 136805 (2010). Medline doi:10.1103/PhysRevLett.105.136805

6. Q. H. Wang, K. Kalantar-Zadeh, A. Kis, J. N. Coleman, M. S. Strano, Electronics and optoelectronics of two-dimensional transition metal dichalcogenides. *Nat. Nanotechnol.* **7**, 699–712 (2012). Medline doi:10.1038/nnano.2012.193

7. J. Feng, X. Qian, C.-W. Huang, J. Li, Strain-engineered artificial atom as a broad-spectrum solar energy funnel. *Nat. Photonics* **6**, 866–872 (2012). doi:10.1038/nphoton.2012.285

8. K. S. Kim, Y. Zhao, H. Jang, S. Y. Lee, J. M. Kim, K. S. Kim, J. H. Ahn, P. Kim, J. Y. Choi, B. H. Hong, Large-scale pattern growth of graphene films for stretchable transparent electrodes. *Nature* **457**, 706–710 (2009). Medline doi:10.1038/nature07719

9. A. K. Geim, I. V. Grigorieva, Van der Waals heterostructures. *Nature* **499**, 419–425 (2013). Medline doi:10.1038/nature12385

10. C. L. Kane, E. J. Mele, Quantum spin Hall effect in graphene. *Phys. Rev. Lett.* **95**, 226801 (2005). Medline doi:10.1103/PhysRevLett.95.226801

11. C. L. Kane, E. J. Mele, Z_2 topological order and the quantum spin Hall effect. *Phys. Rev. Lett.* **95**, 146802 (2005). Medline doi:10.1103/PhysRevLett.95.146802

12. B. A. Bernevig, S.-C. Zhang, Quantum spin Hall effect. *Phys. Rev. Lett.* **96**, 106802 (2006). Medline doi:10.1103/PhysRevLett.96.106802

13. B. A. Bernevig, T. L. Hughes, S.-C. Zhang, Quantum spin Hall effect and topological phase transition in HgTe quantum wells. *Science* **314**, 1757–1761 (2006). Medline doi:10.1126/science.1133734

14. M. König, S. Wiedmann, C. Brüne, A. Roth, H. Buhmann, L. W. Molenkamp, X. L. Qi, S. C. Zhang, Quantum spin hall insulator state in HgTe quantum wells. *Science* **318**, 766–770 (2007). Medline doi:10.1126/science.1148047

15. M. Z. Hasan, C. L. Kane, Colloquium: Topological insulators. *Rev. Mod. Phys.* **82**, 3045–3067 (2010). doi:10.1103/RevModPhys.82.3045

16. X.-L. Qi, S.-C. Zhang, Topological insulators and superconductors. *Rev. Mod. Phys.* **83**, 1057–1110 (2011). doi:10.1103/RevModPhys.83.1057

17. C. Liu, T. L. Hughes, X.-L. Qi, K. Wang, S.-C. Zhang, Quantum spin Hall effect in inverted type-II semiconductors. *Phys. Rev. Lett.* **100**, 236601 (2008). Medline doi:10.1103/PhysRevLett.100.236601

18. L. Du, I. Knez, G. Sullivan, R.-R. Du, Observation of quantum spin Hall states in InAs/GaSb bilayers under broken time-reversal symmetry, http://arxiv.org/abs/1306.1925 (2013).

19. S. Murakami, Quantum spin Hall effect and enhanced magnetic response by spin-orbit coupling. *Phys. Rev. Lett.* **97**, 236805 (2006). Medline doi:10.1103/PhysRevLett.97.236805

20. C.-C. Liu, W. Feng, Y. Yao, Quantum spin Hall effect in silicene and two-dimensional germanium. *Phys. Rev. Lett.* **107**, 076802 (2011). Medline doi:10.1103/PhysRevLett.107.076802

21. D. Xiao, W. Zhu, Y. Ran, N. Nagaosa, S. Okamoto, Interface engineering of quantum Hall effects in digital transition metal oxide heterostructures. *Nat. Commun.* **2**, 596–596 (2011). Medline doi:10.1038/ncomms1602

22. Y. Xu, B. Yan, H. J. Zhang, J. Wang, G. Xu, P. Tang, W. Duan, S. C. Zhang, Large-gap quantum spin Hall insulators in tin films. *Phys. Rev. Lett.* **111**, 136804 (2013). Medline doi:10.1103/PhysRevLett.111.136804

23. H. Weng, X. Dai, Z. Fang, Transition-metal pentatelluride $ZrTe_5$ and $HfTe_5$: A paradigm for large-gap quantum spin Hall insulators. *Phys. Rev. X* **4**, 011002 (2014). http://dx.doi.org/10.1103/PhysRevX.4.011002

24. M. A. Cazalilla, H. Ochoa, F. Guinea, Quantum spin Hall effect in two-dimensional crystals of transition-metal dichalcogenides. *Phys. Rev. Lett.* **113**, 077201 (2014). Medline doi:10.1103/PhysRevLett.113.077201

25. D. Kong, Y. Cui, Opportunities in chemistry and materials science for topological insulators and their nanostructures. *Nat. Chem.* **3**, 845–849 (2011). Medline doi:10.1038/nchem.1171

26. K. Yang, W. Setyawan, S. Wang, M. Buongiorno Nardelli, S. Curtarolo, A search model for topological insulators with high-throughput robustness descriptors. *Nat. Mater.* **11**, 614–619 (2012). Medline doi:10.1038/nmat3332

27. L. Fu, C. L. Kane, Superconducting proximity effect and majorana fermions at the surface of a topological insulator. *Phys. Rev. Lett.* **100**, 096407 (2008). Medline doi:10.1103/PhysRevLett.100.096407

28. L. Fu, C. L. Kane, Josephson current and noise at a superconductor/quantum-spin-Hall-insulator/superconductor junction. *Phys. Rev. B* **79**, 161408 (2009). doi:10.1103/PhysRevB.79.161408

29. J. Alicea, New directions in the pursuit of Majorana fermions in solid state systems. *Rep. Prog. Phys.* **75**, 076501 (2012). Medline doi:10.1088/0034-4885/75/7/076501

30. S. Mi, D. I. Pikulin, M. Wimmer, C. W. J. Beenakker, Proposal for the detection and braiding of Majorana fermions in a quantum spin Hall insulator. *Phys. Rev. B* **87**, 241405 (2013). doi:10.1103/PhysRevB.87.241405

31. J. A. Wilson, A. D. Yoffe, The transition metal dichalcogenides discussion and interpretation of the observed optical, electrical and structural properties. *Adv. Phys.* **18**, 193–335 (1969). doi:10.1080/00018736900101307

32. J. Heising, M. G. Kanatzidis, Exfoliated and restacked MoS_2 and WS_2: Ionic or neutral species? Encapsulation and ordering of hard electropositive cations. *J. Am. Chem. Soc.* **121**, 11720–11732 (1999). doi:10.1021/ja991644d

33. G. Eda, T. Fujita, H. Yamaguchi, D. Voiry, M. Chen, M. Chhowalla, Coherent atomic and electronic heterostructures of single-layer MoS_2. *ACS Nano* **6**, 7311–7317 (2012). Medline doi:10.1021/nn302422x

34. Supplementary materials are available on *Science* Online.

35. L. Fu, C. L. Kane, Topological insulators with inversion symmetry. *Phys. Rev. B* **76**, 045302 (2007). doi:10.1103/PhysRevB.76.045302

36. J. I. Väyrynen, M. Goldstein, L. I. Glazman, Helical edge resistance introduced by charge puddles. *Phys. Rev. Lett.* **110**, 216402 (2013). Medline doi:10.1103/PhysRevLett.110.216402

37. S. Murakami, Phase transition between the quantum spin Hall and insulator phases in 3D: Emergence of a topological gapless phase. *New J. Phys.* **9**, 356 (2007). doi:10.1088/1367-2630/9/9/356

38. J. Wunderlich, B. G. Park, A. C. Irvine, L. P. Zârbo, E. Rozkotová, P. Nemec, V. Novák, J. Sinova, T. Jungwirth, Spin Hall effect transistor. *Science* **330**, 1801–1804 (2010). Medline doi:10.1126/science.1195816

39. D. Pesin, A. H. MacDonald, Spintronics and pseudospintronics in graphene and topological insulators. *Nat. Mater.* **11**, 409–416 (2012). Medline doi:10.1038/nmat3305

40. F. Mahfouzi, N. Nagaosa, B. K. Nikolić, Spin-orbit coupling induced spin-transfer torque and current polarization in topological-insulator/ferromagnet vertical heterostructures. *Phys. Rev. Lett.* **109**, 166602 (2012). Medline doi:10.1103/PhysRevLett.109.166602

41. C. Brüne, A. Roth, H. Buhmann, E. M. Hankiewicz, L. W. Molenkamp, J. Maciejko, X.-L. Qi, S.-C. Zhang, Spin polarization of the quantum spin Hall edge states. *Nat. Phys.* **8**, 486–490 (2012). doi:10.1038/nphys2322

42. C. H. Li, O. M. van 't Erve, J. T. Robinson, Y. Liu, L. Li, B. T. Jonker, Electrical detection of charge-current-induced spin polarization due to spin-momentum locking in Bi_2Se_3. *Nat. Nanotechnol.* **9**, 218–224 (2014). Medline doi:10.1038/nnano.2014.16

43. A. R. Mellnik, J. S. Lee, A. Richardella, J. L. Grab, P. J. Mintun, M. H. Fischer, A. Vaezi, A. Manchon, E. A. Kim, N. Samarth, D. C. Ralph, Spin-transfer torque generated by a topological insulator. *Nature* **511**, 449–451 (2014). Medline doi:10.1038/nature13534

44. C. R. Dean, A. F. Young, I. Meric, C. Lee, L. Wang, S. Sorgenfrei, K. Watanabe, T. Taniguchi, P. Kim, K. L. Shepard, J. Hone, Boron nitride substrates for high-quality graphene electronics. *Nat. Nanotechnol.* **5**, 722–726 (2010). Medline doi:10.1038/nnano.2010.172

45. J. Liu, T. H. Hsieh, P. Wei, W. Duan, J. Moodera, L. Fu, Spin-filtered edge states with an electrically tunable gap in a two-dimensional topological crystalline insulator. *Nat. Mater.* **13**, 178–183 (2014). Medline doi:10.1038/nmat3828

46. P. Michetti, B. Trauzettel, Devices with electrically tunable topological insulating phases. *Appl. Phys. Lett.* **102**, 063503 (2013). doi:10.1063/1.4792275

47. M. Calandra, Chemically exfoliated single-layer MoS_2: Stability, lattice dynamics, and catalytic adsorption from first principles. *Phys. Rev. B* **88**, 245428 (2013). doi:10.1103/PhysRevB.88.245428

48. P. Hohenberg, W. Kohn, Inhomogeneous electron gas. *Phys. Rev. B* **136** (3B), B864–B871 (1964). doi:10.1103/PhysRev.136.B864

49. W. Kohn, L. Sham, Self-consistent equations including exchange and correlation effects. *Phys. Rev.* **140** (4A), A1133 (1965). doi:10.1103/PhysRev.140.A1133

50. G. Kresse, J. Furthmuller, Efficiency of ab-initio total energy calculations for metals and semiconductors using a plane-wave basis set. *Comput. Mater. Sci.* **6**, 15–50 (1996). doi:10.1016/0927-0256(96)00008-0

51. G. Kresse, J. Furthmuller, Efficient iterative schemes for ab initio total-energy calculations using a plane-wave basis set. *Phys. Rev. B* **54**, 11169–11186 (1996). doi:10.1103/PhysRevB.54.11169

52. P. E. Blöchl, Projector augmented-wave method. *Phys. Rev. B* **50**, 17953–17979 (1994). doi:10.1103/PhysRevB.50.17953

53. J. P. Perdew, K. Burke, M. Ernzerhof, Generalized gradient approximation made simple. *Phys. Rev. Lett.* **77**, 3865–3868 (1996). Medline doi:10.1103/PhysRevLett.77.3865

54. D. C. Langreth, M. J. Mehl, Beyond the local-density approximation in calculations of ground-state electronic properties. *Phys. Rev. B* **28**, 1809–1834 (1983). doi:10.1103/PhysRevB.28.1809

55. A. D. Becke, Density-functional exchange-energy approximation with correct asymptotic behavior. *Phys. Rev. A* **38**, 3098–3100 (1988). Medline doi:10.1103/PhysRevA.38.3098

56. H. Monkhorst, J. Pack, Special points for Brillouin-zone integrations. *Phys. Rev. B* **13**, 5188–5192 (1976). doi:10.1103/PhysRevB.13.5188

57. L. Hedin, New method for calculating the one-particle Green's function with application to the electron-gas problem. *Phys. Rev.* **139** (3A), A796–A823 (1965). doi:10.1103/PhysRev.139.A796

58. M. S. Hybertsen, S. G. Louie, Electron correlation in semiconductors and insulators: Band gaps and quasiparticle energies. *Phys. Rev. B* **34**, 5390–5413 (1986). doi:10.1103/PhysRevB.34.5390

59. M. P. L. Sancho, J. M. L. Sancho, J. Rubio, Highly convergent schemes for the calculation of bulk and surface Green functions. *J. Phys. F* **15**, 851–858 (1985). doi:10.1088/0305-4608/15/4/009

60. N. Marzari, D. Vanderbilt, Maximally localized generalized Wannier functions for composite energy bands. *Phys. Rev. B* **56**, 12847–12865 (1997). doi:10.1103/PhysRevB.56.12847

61. X. Qian, J. Li, L. Qi, C.-Z. Wang, T.-L. Chan, Y.-X. Yao, K.-M. Ho, S. Yip, Quasiatomic orbitals for ab initio tight-binding analysis. *Phys. Rev. B* **78**, 245112 (2008). doi:10.1103/PhysRevB.78.245112

62. T. Fukui, Y. Hatsugai, Quantum spin Hall effect in three dimensional materials: Lattice computation of Z_2 topological invariants and its application to Bi and Sb. *J. Phys. Soc. Jpn.* **76**, 053702 (2007). doi:10.1143/JPSJ.76.053702